PAPER

Check for updates

A data-driven computational scheme for the nonlinear mechanical properties of cellular mechanical metamaterials under large deformation†

Tianju Xue, [ID] *[a] Alex Beatson,[b] Maurizio Chiaramonte,*[c] Geoffrey Roeder,[b] Jordan T. Ash,[b] Yigit Menguc,[c] Sigrid Adriaenssens,[a] Ryan P. Adams[b] and Sheng Mao [ID] *[de]

Cellular mechanical metamaterials are a special class of materials whose mechanical properties are primarily determined by their geometry. However, capturing the nonlinear mechanical behavior of these materials, especially those with complex geometries and under large deformation, can be challenging due to inherent computational complexity. In this work, we propose a data-driven multiscale computational scheme as a possible route to resolve this challenge. We use a neural network to approximate the effective strain energy density as a function of cellular geometry and overall deformation. The network is constructed by "learning" from the data generated by finite element calculation of a set of representative volume elements at cellular scales. This effective strain energy density is then used to predict the mechanical responses of cellular materials at larger scales. Compared with direct finite element simulation, the proposed scheme can reduce the computational time up to two orders of magnitude. Potentially, this scheme can facilitate new optimization algorithms for designing cellular materials of highly specific mechanical properties.

1 Introduction

Cellular mechanical metamaterials (CMMs) with repeating cells are commonly observed in both nature and industry, from biological materials such as honeycombs to synthetic structures such as metallic microlattices. These materials can exhibit unique mechanical properties, such as high stiffness- and/or strength-to-density ratio,[1] that are primarily determined by geometries. Traditionally, the study of this field is limited to several simple structures and under relatively small deformation.[2] Yet in the past decade, the advent of fabrication technologies such as additive manufacturing[3,4] has enabled precise but fast realization of sophisticated cellular architectures made of soft materials,

such as elastomers. These materials not only can bear large deformation, but also exhibit novel mechanical properties under that condition, including negative Poisson's ratio (auxeticity),[5–7] shape morphing,[8] tunable bandstructures[9] and energy absorption.[10] These novel properties have created an avenue for many exciting engineering applications, *e.g.*, soft actuators, materials with *in situ* tunable functionalities, reusable energy-absorbing materials, *etc.*[11–16]

The rapid development on the fabrication side demands a fast and predictive computational method to predict the mechanical behaviors of CMMs. For materials with a relatively small number of cells, one can conduct a direct numerical simulation (DNS) on the whole specimen using the finite element method (FEM).[17] However, the mechanical behaviors of soft CMMs are often highly nonlinear and may involve mechanical instability, thus requiring a fine spatiotemporal resolution for DNS calculations. DNS can easily become computationally intractable as CMMs usually consist of a large number of cells. Alternatively, one can conduct a fine-mesh FEM calculation on a representative volume element (RVE), often composed of one or several repeating cells,[6] by prescribing appropriate boundary conditions. Such a method can efficiently predict the mechanical response of CMMs under homogeneous deformation. When CMMs are subject to complex loads, such predictions will fail.

[a] *Department of Civil and Environmental Engineering, Princeton University, Princeton, NJ 08544, USA. E-mail: txue@princeton.edu*

[b] *Department of Computer Science, Princeton University, Princeton, NJ 08544, USA*

[c] *Facebook Reality Labs, Redmond, WA, 98052, USA. E-mail: mchiaram@fb.com*

[d] *Department of Mechanics and Engineering Science, BIC-ESAT, College of Engineering, Peking University, Beijing 100871, People's Republic of China. E-mail: maosheng@pku.edu.cn*

[e] *Department of Mechanical and Aerospace Engineering, Princeton University, Princeton, NJ 08544, USA*

† Electronic supplementary information (ESI) available. See DOI: 10.1039/d0sm00488j

When the size of the CMM is much larger than that of the repeating cells, multiscale analysis such as homogenization can be a useful tool. Homogenization, often called "coarse-graining" in the physics community, is often used to predict the macroscopic behavior of composites from their micro-structures.[18,19] The early development of homogenization primarily focuses on the analytical approach. Following the pioneering work of Eshelby,[20] various analytical homogenization methods have been developed for linear materials[21–26] and later extended to nonlinear materials.[27–30] While these analytical approaches provide useful bounds, they are less accurate when microstruc-tures become sophisticated.[31] Computational homogenization is more suitable in this scenario. Reviews of the recent progress in this field can be found in ref. 32–34. Among various methods of computational homogenization, two main categories can be distinguished: concurrent and off-line methods. Concurrent methods integrate the macro- and micro-scale problems through proper mathematical formulations and solve both problems concurrently. For example, the FE^2 method is a widely adopted concurrent scheme, and uses FEM to solve problems at both scales.[35–40] Another example is given by the spectral method based on Fast Fourier Transform (FFT).[41–44] Concurrent methods are powerful and accurate, yet can still be computationally expensive, mainly due to the nested numerical solvers needed to balance calculations at both scales. On the other hand, for off-line methods, the macro- and micro-scale problems are solved separately. Effective constitutive laws are first constructed based on a set of numerical calculations at microscales, and then used to solve problems at macro-scales.[45,46] Thus, offline methods can avoid the huge cost of nested numerical solvers and in some cases be orders of magnitude faster than the concurrent methods.[46,47] Essentially, the constitutive relation can be seen as a multi-dimensional mapping from the microstructural features to the macroscopic response of the material, and the core of offline methods is to efficiently and accurately construct such a mapping. To this end, several techniques[46–52] have been developed, including recent efforts using neural networks.[53,54]

Neural networks (NNs) are massively parametric function approximators inspired by biological neural networks.[55] Given a large number of input/output examples, neural networks can often successfully learn functions on high-dimensional spaces. This process of "learning" the function corresponds to identi-fying an optimal set of parameters, i.e., neural network "weights", to capture the relationship between inputs and outputs reflected in the training data. Neural networks have been demonstrated to be powerful function approximators for solving challenging engineering tasks, such as language modeling,[56] image classification,[57] and machine translation.[58] More recently, there has been a growing interest in applying neural networks to complex problems in natural sciences, e.g., physics,[59–61] chemistry,[62] astronomy,[63] biomedicine,[64] and materials science.[65–69]

In the present work, we extend previous works on NN-based computational homogenization methods[53,54] to model the non-linear mechanical behavior of cellular mechanical metamaterials under large deformation. For that purpose, we first generate training data by conducting a large number of RVE calculations at the cellular scale. We then train a neural network on those data to approximate the effective strain energy density at the macro-scale, which is a function of the macroscopic strain and microscopic structural parameters. Through this NN-based surro-gate model for effective strain energy density, the coarse-grained constitutive relations can be easily obtained, which greatly reduces the computational cost of determining the mechanical behavior of cellular materials at the macro-scale.

This paper is organized as follows. In Section 2, the finite deformation theory of hyperelastic cellular mechanical meta-materials and the specific geometries of this study are described. In Section 3, we propose a neural network-based multiscale computational scheme to determine the mechanical responses of CMMs and describe the procedures to carry out the scheme in Section 4. Numerical examples are presented in Section 5, where our NN-based method is compared with DNS in terms of accuracy and efficiency. In Section 6, we discuss the applicability and the limitations of our NN-based method. Finally we conclude in Section 7.

2 Problem formulation

2.1 Finite deformation elasticity

Consider a homogeneous elastic body in a 3D Euclidean space $\mathbb{R}^3$, where we introduce a fixed Cartesian coordinate system with orthonormal basis $\{e_1,e_2,e_3\}$. In an unstressed state, the body occupies a region $\mathbb{B} \subset \mathbb{R}^3$ (reference configuration) with a boundary $\partial\mathbb{B}$ whose outward normal is $\boldsymbol{N}$. Upon mechanical loading, the body deforms and occupies a different region $\mathbb{B}_t \subset \mathbb{R}^3$ (deformed configuration). Deformation can therefore be described as a mapping: $\boldsymbol{\varphi} \colon \mathbb{B} \to \mathbb{B}_t$, which maps any material point $\boldsymbol{X} \in \mathbb{B}$ to its counterpart $\boldsymbol{x} \in \mathbb{B}_t$, i.e. $\boldsymbol{x} = \boldsymbol{\varphi}(\boldsymbol{X})$. The corresponding displacement field is defined as $\boldsymbol{u} = \boldsymbol{x} - \boldsymbol{X}$ and the deformation gradient $\boldsymbol{F} = \dfrac{\partial \boldsymbol{x}}{\partial \boldsymbol{X}}$. We denote vectors and tensors with a bold font in contrast to scalars with a normal font.

The constitutive model of a hyperelastic material can be defined by a strain energy density function (per volume) W, which depends on $\boldsymbol{F}$, through the right Cauchy–Green tensor $\boldsymbol{C} = \boldsymbol{F}^T\boldsymbol{F}$. The displacement field $\boldsymbol{u}$ can be determined by solving for the stationary point $\delta\Psi = 0$ of the following functional (in the absence of body force):

$$\Psi(\boldsymbol{u}) = \int_{\mathbb{B}} W(\boldsymbol{F})\mathrm{d}\boldsymbol{X} - \int_{\partial\mathbb{B}^N} \boldsymbol{u} \cdot t \,\mathrm{d}\boldsymbol{S}, \qquad (1)$$

with $\boldsymbol{u} = \boldsymbol{u}_b$ and $\delta\boldsymbol{u} = 0$ on $\partial\mathbb{B}^D$, where $\boldsymbol{u}_b$ is the prescribed displacement field, t is the prescribed traction (force per unit reference area), $\partial\mathbb{B}^N \cup \partial\mathbb{B}^D = \partial\mathbb{B}$ and $\partial\mathbb{B}^N \cap \partial\mathbb{B}^D = \varnothing$. The measures $\mathrm{d}\boldsymbol{X}$ and $\mathrm{d}\boldsymbol{S}$ are the infinitesimal volume and surface elements in the reference configuration respectively. Alterna-tively, the above variational problem can be formulated as a boundary value problem:

$$\mathrm{Div}\,\boldsymbol{P} = \boldsymbol{0} \quad \text{in } \mathbb{B},$$

$$\boldsymbol{u} = \boldsymbol{u}_\text{b} \quad \text{on } \partial\mathbb{B}^D,$$

$$\boldsymbol{P}\cdot\boldsymbol{N} = \boldsymbol{t} \quad \text{on } \partial\mathbb{B}^N, \qquad (2)$$

where Div is the divergence operator in the reference configuration and $\boldsymbol{P} = \dfrac{\partial W}{\partial \boldsymbol{F}}$ is the first Piola–Kirchoff stress. These problems can be numerically solved by FEM.

The formulation described above is applicable to any hyperelastic material, but in this work we focus on CMMs made of soft elastomers and therefore adopt the following form of W:

$$W = \frac{\mu}{2}(J^{-2/3}I_1 - 3) + \frac{\kappa}{2}(J - 1)^2, \qquad (3)$$

where $J = \det(\boldsymbol{F})$ and $I_1 = \text{tr}(\boldsymbol{C})$; $\mu = \dfrac{E}{2(1 + \nu)}$ and $\kappa = \dfrac{E}{3(1 - 2\nu)}$ denote the initial shear and bulk moduli, respectively, with E and ν being the material's Young's modulus and Poisson's ratio. The above W is commonly used to model isotropic elastomers that are almost incompressible and we assume $\nu = 0.3$ throughout this work.

2.2 Problem geometry

In this work, we focus on a special but widely used class of CMMs: 2D porous cellular solids with a repeating unit cell. We adopt a plane strain setting here, i.e., $u_i = u_i(X_1, X_2)$, $i = 1,2$ and $u_3 = 0$. Previous works[6,7] have shown that the mechanical properties of these CMMs highly depend on the shape of the pore. Following previous treatments, our study focuses on pores with four-fold symmetry whose contour can be described by the following parametrization:

$$r(\theta) = r_0(1 + \xi_1 \cos(4\theta) + \xi_2 \cos(8\theta)), \qquad (4)$$

where r and θ are the polar radius and polar angle respectively. By changing the parameters $\boldsymbol{\xi} = (\xi_1, \xi_2)$, we get a family of different pore shapes as illustrated in Fig. 1. Specifically in this work, we focus on square arrays of these unit cells and therefore, for a material with a unit cell length of L_0, its porosity ϕ_0 is uniquely determined by r_0 and $\boldsymbol{\xi}$ via the relation $\phi_0 = \dfrac{\pi}{2}(r_0/L_0)^2(\xi_1{}^2 + \xi_2{}^2 + 2)$. In this work, we fix $L_0 = 0.5$ and porosity $\phi_0 = 0.5$.

Among all the possible pore shapes, we focus on two types (A and B in Fig. 1): pore A is circular, with $\boldsymbol{\xi}_A = (0, 0)$, and pore B breaks the angular symmetry, with $\boldsymbol{\xi}_B = (-0.2, 0.2)$. We choose these two shapes as our representative examples for two reasons. First, mechanical instability can be triggered in CMMs made of both unit cells under compression, which leads to an asymmetric mechanical response of the CMMs under tension and compression. Second, even though mechanical instability can be triggered in these two CMMs, they still exhibit very distinct mechanical responses under the same mechanical loading.[6,7]

3 NN-based multiscale approach

Direct numerical simulation of cellular mechanical metamaterials made of large numbers of unit cells is challenging, especially for
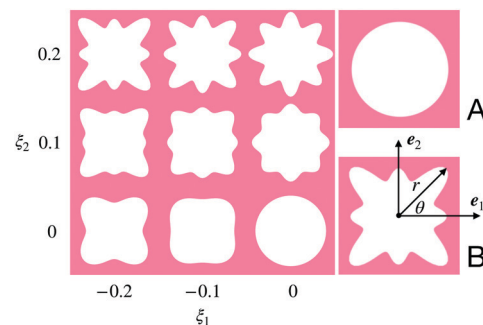

Fig. 1 Left: A map from the parameters to the pore shapes indicated by eqn (4). For each (ξ_1, ξ_2), we get a corresponding pore shape. Right: The two representative pore shapes studied in this work.

CMMs with complicated cellular geometries or that undergo large deformation, mainly due to the large computational cost. The computational expense arises from two factors. First, to resolve detailed cellular geometries, the finite element mesh size must be no larger than microstructural features. Second, since the mechanical responses can be highly nonlinear under large deformation, small time steps are required for DNS to converge. To address these issues, we adopt a multiscale approach called (offline) computational homogenization,[53,54] which performs fine-mesh FEM calculations at the RVE level to obtain the coarse-grained constitutive relations, and then uses these relations to predict the mechanical behavior of the material at larger scale.

Our computational homogenization approach starts with a study of the representative volume element of the CMM. The choice of RVE is not unique, but it has to be simultaneously large enough to capture the influence of cellular geometries on the overall mechanical behavior and small enough to be considered as a material point for the CMM. For example, as shown in Fig. 2, for a CMM composed of many unit cells with pore A, we have chosen ABCD, a 2×2 array of unit cells, as our RVE. This choice of RVE ensures that we capture the mechanical instability that leads to reorganization of the neighboring unit cells.[6,7] We emphasize that the above statement relies on the critical assumption of separation of length scales, i.e. the size of the CMM is much larger than that of the unit cell and RVE, without which the homogenization approach is invalid.
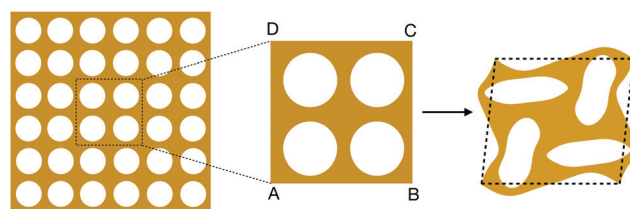

Fig. 2 A 2×2 RVE taken from a cellular porous structure with repeating units. Followed by the arrow is an example showing the periodic boundary conditions applied to the RVE. Here we specify a macroscopic displacement gradient $\bar{\boldsymbol{H}} = \begin{bmatrix} 0 & 0.2 \\ 0 & -0.2 \end{bmatrix}$. The deformed configuration (rightmost) shows the resulted displacement field of this RVE: $\boldsymbol{u} = \bar{\boldsymbol{H}}\cdot\boldsymbol{X} + \boldsymbol{u}^*$ with $\boldsymbol{u}^*$ being the periodic fluctuation. The dashed profile shows the deformation corresponding to the applied overall displacement $\bar{\boldsymbol{u}} = \bar{\boldsymbol{H}}\cdot\boldsymbol{X}$.

To construct the effective strain energy density of this RVE, we conduct a fine-mesh FEM calculation on the RVE under macroscopic deformations $\bar{F}$ by prescribing the following periodic boundary conditions:

$$u(X) = (\bar{F} - I)\cdot X + u^*(X) = \bar{H}\cdot X + u^*(X), \qquad (5)$$

where I is the identity tensor and $\bar{H}$ denotes the macroscopic displacement gradient. $\bar{F}$ and $\bar{H}$ are uniform on the RVE and periodic boundary conditions are applied to ensure $\int_{\partial V} n \otimes u^* = 0$. For example, for the RVE ABCD in Fig. 2, we have $u^*_{AD} = u^*_{BC}$ and $u^*_{AB} = u^*_{DC}$. Essentially, eqn (5) decomposes the total displacement of the RVE into a macroscopic (overall) part $\bar{u} = \bar{H}\cdot X$ and a microscopic (fluctuating) part u^*.

The effective strain energy density $\overline{W}$ can be obtained *via* the average W over the RVE: $\overline{W} = V^{-1}\int_V W dV$ with V being the total volume of the RVE (for plane strain, $dV = dX_1 dX_2$). Other macroscopic quantities can be obtained in the same fashion. This effective strain energy density $\overline{W}$ is the bridge that connects the microscopic features to macroscopic mechanical responses. In essence, $\overline{W}$ should be a function of $\bar{F}$ as well as the microstructural features ξ: $\overline{W} = \overline{W}(\bar{F}, \xi)$. Once that relation is established, we then treat the RVE as a material point in the CMM and use FEM to find the approximate solution to the stationary point of the following functional:

$$\overline{\Psi}(\bar{u}) = \int_{\mathbb{B}} \overline{W}(\bar{F}, \xi) dX - \int_{\partial\mathbb{B}^N} \bar{u} \cdot \bar{t}\, dS, \qquad (6)$$

with $\bar{u} = \bar{u}_b$ and $\delta\bar{u} = 0$ on $\partial\mathbb{B}^D$. Making use of the celebrated Hill–Mandel condition[70] $\bar{P} = \dfrac{\partial \overline{W}}{\partial \bar{F}}$, the above minimization formulation can be shown to be equivalent to the following macroscopic BVP:

$$\text{Div}\, \bar{P} = 0 \quad \text{in } \mathbb{B},$$

$$\bar{u} = \bar{u}_b \quad \text{on } \partial\mathbb{B}^D,$$

$$\bar{P}\cdot N = \bar{t} \quad \text{on } \partial\mathbb{B}^N. \qquad (7)$$

Therefore, the key to this computational homogenization scheme is to construct $\overline{W}$ as a function of $\bar{F}$ (more strictly speaking $\bar{C}$) and ξ. In this work, we adopt a data-driven approach based on neural networks.

Neural networks (NNs) are powerful computational structures for constructing massively parametric mappings.[55] The classic general form of a neural network is the multi-layer perceptron (MLP), made up of fully connected layers.[71] The input vector x is processed through several hidden layers and finally to an output vector y. Suppose that the ith layer has m nodes and the $i + 1$ layer has n of them, the computation between these two layers is given by $y^i = f^i(x^i) := \sigma(w^i\cdot x^i + b^i)$, where $w^i \in \mathbb{R}^{n\times m}$ and $b^i \in \mathbb{R}^m$ are the weight matrix and bias vector of the ith layer, and σ is an element-wise nonlinear function, such as a logistic function $\sigma(y) = 1/(1 + e^{-y})$ or tanh. We can "stack" these transformations as $y = f^k(x^k) = f^k \circ f^{k-1}(x^{k-1}) = \ldots = f^k \circ \ldots \circ f^1(x)$ for a MLP with $k - 1$ hidden layers. We hereby denote this mapping as $y = f_\theta(x)$ to emphasize that this mapping is under the parameter
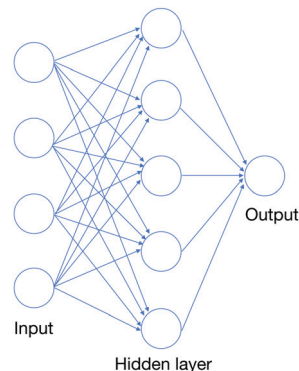

Fig. 3 An MLP with one hidden layer. The neural network function takes an input vector and performs an affine transformation followed by a non-linear activation function on the input vector, producing an intermediate vector at the hidden layer. A similar transformation on the intermediate vector then yields the output of the neural network function.

$\theta = (w^1, w^2, \ldots, w^k; b^1, b^2, \ldots, b^k)$. A typical MLP with only one hidden layer is shown in Fig. 3.

The weight matrices and bias vectors θ are called the parameters of the neural network and they are optimized through a training procedure that minimizes a loss function reflecting the quality of the fit to data. This training is typically performed *via* a stochastic optimization procedure such as stochastic gradient descent.[72] At each step, one randomly selects a subset of the training examples x each with the corresponding target value y^* and computes a loss function $\mathscr{L}(y^*, y)$ (for example, the squared Euclidean distance between targets and predictions $\|y^* - y\|_2^2$). Gradients of this loss function with respect to the parameters are then computed using reverse-mode automatic differentiation and the parameters are updated accordingly.[73] This proceeds until a convergence criterion is achieved. After training and other validation and calibration processes, we can then deploy the neural network to make predictions for new inputs.

In this work, we use an MLP to approximate the effective strain energy density, namely $\overline{W}_{NN}(\bar{C}, \xi) \approx \overline{W}(\bar{C}, \xi)$. The input vector is a 5-dimensional vector: $x = (\bar{C}_{11}, \bar{C}_{12}, \bar{C}_{22}, \xi_1, \xi_2)$ and the output is a scalar $y = \overline{W}_{NN}$. For any given input, the target output is generated by RVE calculations. The goal is to train an MLP which can reproduce the results of these calculations for out-of-sample vectors. After training the MLP, we replace the $\overline{W}$ in eqn (6) with $\overline{W}_{NN}$ and solve the macroscopic problem.

We use scikit-learn,[74] an open source machine learning framework, to build, train and later test our neural network. All finite element calculations are carried out using an open-source FEM package FEniCS.[75]
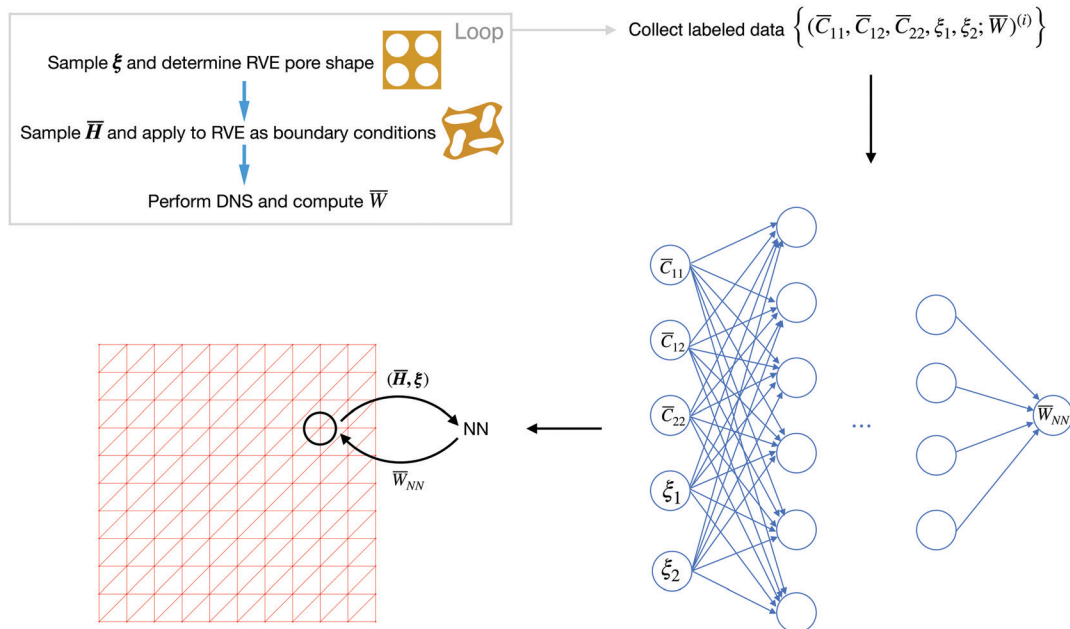
4 Construction of the NN-based computational homogenization scheme

In the previous section, we have outlined an NN-based multi-scale computational homogenization scheme, with the goal of obtaining a mapping from macroscopic deformation $\bar{C}$ and

Fig. 4 The data-driven computational homogenization procedure consists of three steps: (1) building the offline training database by performing RVE calculations at the cellular level; (2) training the neural network to obtain a surrogate model for effective strain energy density; and (3) deploying the NN-based surrogate model for macroscopic problems.

microstructural parameters ξ to the effective strain energy density $\overline{W}$. This scheme, as illustrated in Fig. 4, mainly consists of three steps: (1) offline construction of training data, (2) optimization of neural network parameters, and (3) deployment of the NN-based surrogate model for FEM at the macro-scale. In this section, we will describe these steps in detail.

4.1 Offline generation of training data

As mentioned above, the first step of constructing the NN-based multiscale computational scheme is to construct a proper training database composed of labeled data, each in the form of an input vector and its target output: $\{(\overline{C}_{11}, \overline{C}_{12}, \overline{C}_{22}, \xi_1, \xi_2; \overline{W})^{(i)}\}$. The target output $\overline{W}^{(i)}$ is obtained *via* finite element calculation of the RVE with the corresponding geometric parameters $\xi^{(i)}$ and subject to the corresponding macroscopic field of $\overline{C}^{(i)}$.

In this work, we focus on CMMs composed of two types of unit cells: those with pore A and pore B, so the choice of $\xi^{(i)}$ is limited: $\xi^{(i)} \in \{\xi_A, \xi_B\}$. However, the choice of the macroscopic field $\overline{C}^{(i)}$ is in principle infinite since it varies continuously. Therefore some care is necessary in constructing an effective sampling method for $\overline{C}^{(i)}$.

First we must identify a domain over which $\overline{C}^{(i)}$ is to be sampled. Such a region should cover the nonlinear mechanical behaviors of primary interest. For example, for CMMs composed of unit cells with pore A, beyond certain compression the CMM undergoes mechanical instability which leads to auxetic behavior. This behavior can be observed for $\overline{H}_{22} = -0.125$, $\overline{H}_{12} = \overline{H}_{21} = 0$ and $\overline{H}_{11} \in [-0.08, 0.08]$, as shown in Fig. 5a.

The effective Poisson's ratio is calculated to be $\bar{\nu} = -0.26$ (defined as $-\dfrac{\overline{H}_{11}}{\overline{H}_{22}}$ at the star point, where $\dfrac{\partial \overline{W}}{\partial \overline{F}_{11}} = \overline{P}_{11} = 0$). As for CMMs made of unit cells with pore B, when subject to both shear and compression, mechanical instability can lead to the bifurcation of microstructures.[7] This is observed when $\overline{H}_{22} = -0.125$, $\overline{H}_{11} = \overline{H}_{21} = 0$ and $\overline{H}_{12} \in [-0.7, 0.7]$. As shown in Fig. 5b, a double well shape of $\bar{W}$ is observed as a function of $\overline{H}_{12}$ with two energy minima. Therefore, when the CMM is subject to an overall compression $\overline{H}_{22} = -0.125$, the CMM will bifurcate into two different microstructures that correspond to these two minima.

The inspections above offer insight into a reasonable range of $\overline{H}$ for sampling data. The range should be sufficiently wide so that important mechanics are reflected in the database, while it should also be limited so that undesired behaviors like self-contact are avoided with the current FEM simulation. The sampling region chosen for pore A is

$$\{-0.2 \leq \overline{H}_{11} \leq 0.2, \ -0.2 \leq \overline{H}_{12} \leq 0.2,$$
$$-0.2 \leq \overline{H}_{21} \leq 0.2, \ -0.2 \leq \overline{H}_{22} \leq 0.2\}, \quad (8)$$

and that for pore B:

$$\{-0.2 \leq \overline{H}_{11} \leq 0.2, \ -0.8 \leq \overline{H}_{12} \leq 0.8,$$
$$-0.8 \leq \overline{H}_{21} \leq 0.8, \ -0.2 \leq \overline{H}_{22} \leq 0.2\}. \quad (9)$$

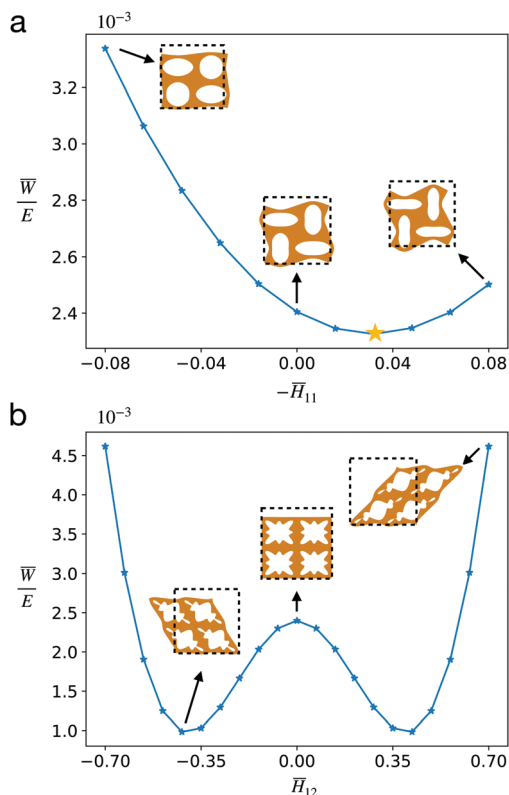We adopted Sobol sequences[76] to generate 5000 different samples from each of the above regions. Such a sequence is

Fig. 5 Effective strain energy density $\overline{W}$ (normalized by E) under different $\overline{H}$ obtained from RVE calculations for unit cells with pore A and pore B: (a) $\overline{W}/E$ versus $\overline{H}_{11}$ for pore A and (b) $\overline{W}/E$ versus $\overline{H}_{12}$ for pore B.

often used to generate sparse yet representative samples that are evenly distributed over the given region. To maximize the speed of data collection, we conducted a mesh refinement study to obtain the optimal mesh size under a reasonable tolerance (see ESI†). On a personal computer with a 3.2 GHz Intel Core i7 CPU and 16GB memory, it took about 20 hours to complete the process of data collection.

4.2 Neural network training

Once the database is constructed, the next step is to train a neural network to establish a mapping from input vector $\boldsymbol{x} = (\overline{C}_{11}, \overline{C}_{12}, \overline{C}_{22}, \xi_1, \xi_2)$ to its target scalar output $y = \overline{W}$. We randomly split our database into a training set (90% of the data) and a test set (the rest 10%). Our neural networks will be trained on the training set and the test set is used to ensure good generalizability and avoid overfitting.

The neural network used here is an MLP with one hidden layer, which as we will show later is able to provide sufficient accuracy for our problem. The logistic function $\sigma(y) = 1/(1 + e^{-y})$ is chosen as our activation function, and mean squared error (MSE) is chosen as our loss function: $\text{MSE} = \sum_{i=1}^{n} (\hat{y}^{(i)} - y^{(i)})^2/n$, where n is the number of data points evaluated and $\hat{y}^{(i)}$ denotes the output of the MLP given input $\boldsymbol{x}^{(i)}$. The neural network is trained using mini-batch stochastic gradient descent with Adam optimizer.[77] Hyperparameters such as number of

neurons in the hidden layer are first optimized via k-fold cross-validation[78] (see ESI†). We obtained the following optimal hyperparameters: learning rate 10^{-2}, batch size 64, and 128 neurons in the hidden layer. We then train our neural networks using these hyperparameters. The training time for the NN is typically within 1 minute on a personal computer. After training of 1000 epochs, our NN model reports a training MSE of 6.11×10^{-5} and a test MSE of 7.67×10^{-5}.

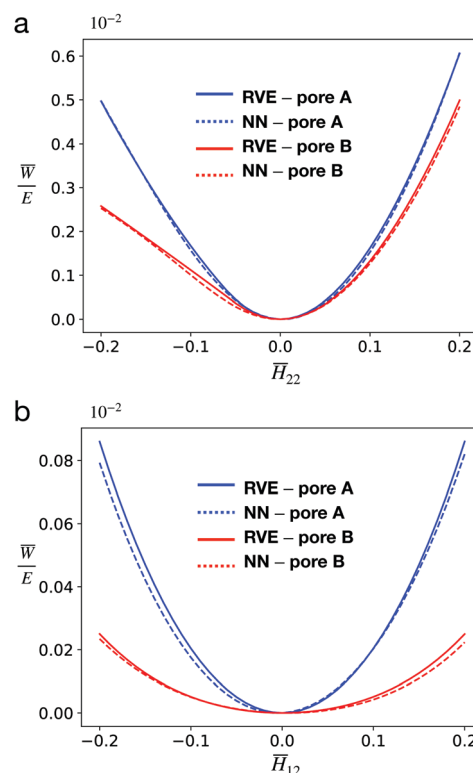We performed polynomial regression on the same data set as a baseline comparison. As shown in Fig. 7, when the

Fig. 6 Comparisons of the normalized effective strain energy densities obtained via RVE calculation (solid line) and trained NN model (dashed line) for both pore A (blue) and pore B (red) on the two benchmarks: (a) uniaxial strain and (b) simple shear strain.
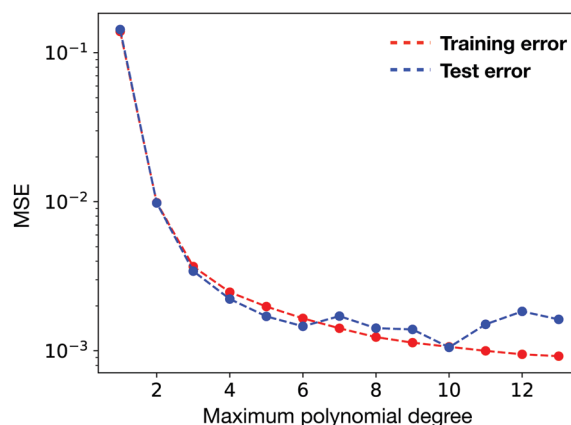

Fig. 7 Training and test MSE for polynomial regression.

maximum degree of polynomial is increased, the MSE tends to decrease. But when the maximum degree exceeds 10, the regression problem starts to become ill-conditioned and thus results in large MSE.[79] The best of polynomial regression reports a test error of 1.05×10^{-3}, which is more than an order of magnitude larger than the neural network model.

We further validate our NN model in two test cases to serve as our benchmarks by prescribing the following $\bar{H}$:

(1) Uniaxial strain: $\bar{H}_{11}, \bar{H}_{12}, \bar{H}_{21} = 0, \bar{H}_{22} \neq 0$

(2) Simple shear strain: $\bar{H}_{11}, \bar{H}_{21}, \bar{H}_{22} = 0, \bar{H}_{12} \neq 0$

We conducted the above two test cases on both unit cells with pore A and pore B and ensured that the $\bar{H}$'s tested here are different from those in the database. The results are shown in Fig. 6, where the effective strain energy obtained *via* RVE calculation and that from the NN model are compared. It is observed that the NN model agrees with the RVE calculation reasonably well. The errors between NN model and RVE calculation are also small among both benchmarks: the respective MSEs are 2.42×10^{-5} and 4.28×10^{-5}.

4.3 Deployment of the NN-based surrogate model

Now that we have obtained an optimized NN model of the effective strain energy density $\overline{W}_{\text{NN}}$, we replace the $\overline{W}$ in eqn (6) with the obtained $\overline{W}_{\text{NN}}$. Then, for any given ξ, the solution to the macroscopic problem boils down to finding the stationary point $\delta\overline{\Psi}_{\text{NN}} = 0$ of the following functional:

$$\overline{\Psi}_{\text{NN}}(\bar{u}) = \int_{\mathbb{B}} \overline{W}_{\text{NN}}\left[\overline{C}(\bar{u}), \xi\right] \mathrm{d}X - \int_{\partial\mathbb{B}^N} \bar{u} \cdot \bar{t}\, \mathrm{d}S, \qquad (10)$$

with $\bar{u} = \bar{u}_{\text{b}}$ and $\delta\bar{u} = 0$ on $\partial\mathbb{B}^D$.

By extracting out the optimal parameters of the NN model, the explicit functional form of $\overline{W}_{\text{NN}}(\overline{C}, \xi)$ is readily available, which can be computed iteratively as described in Section 3. However, to find the stationary point of the above functional $\overline{\Psi}_{\text{NN}}$, one needs to efficiently evaluate the derivatives of $\overline{\Psi}_{\text{NN}}$ to compute quantities like the first Piola–Kirchhoff stress $\overline{P}_{\text{NN}} = \dfrac{\partial\overline{W}_{\text{NN}}}{\partial\overline{F}}$ as well as the tangent stiffness tensor $\mathbb{K} = \dfrac{\partial\overline{P}_{\text{NN}}}{\partial\overline{F}}$. In this work, we made use of the automatic symbolic differentiation feature provided by the open-source package FEniCS (specifically the UFL component[80] of the package) to compute those derivatives. The standard Newton–Raphson method is used to find the root of the nonlinear equations. We use automatic differentiation and other features of FEniCS, so that the code can be written in a concise and near-math fashion, which provides an easier access to broader audiences. Equivalently, the exact same derivatives could be computed analytically[53] or *via* finite differences.[54]

5 Numerical examples

In this section, we employed the aforementioned NN-based multiscale approach to study the mechanical behavior of CMMs composed of 2D arrays of cells with different pore shapes and
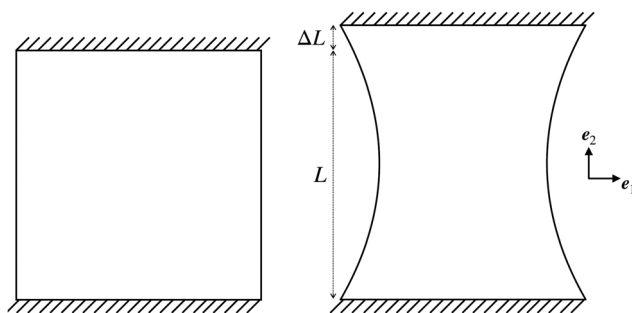

Fig. 8 Boundary conditions for uniaxial tests. The upper and lower sides of the plate have fixed displacement conditions while the left and right sides are traction free.

compare that with direct numerical simulation. As shown in Fig. 8, a square-shaped CMM with a length $L = 16L_0$ is studied. The CMM is subject to a uniaxial testing with displacement control. Specifically, a displacement ΔL along the $\mathbf{e}_2$ direction is applied at the top with the bottom kept fixed, while the left and right sides of the CMM remain traction free. This uniaxial testing is a standard practice to obtain the stress–strain curve of materials. Here, the engineering strain ε and engineering stress σ of the CMM are defined as follows: $\varepsilon = \dfrac{\Delta L}{L}$ and $\sigma = \dfrac{F}{L}$, where $F = \int_{\text{top}} P_{22}\mathrm{d}X_1$ is the total resultant force (per thickness) on the top surface.

We perform this uniaxial test on a CMM with spatially uniform pore shapes of either pore A or pore B. Previous studies[76] suggested that compression can lead to distinct mechanical behaviors of these two CMMs. This phenomenon is indeed observed in Fig. 9, where the deformed shapes of the

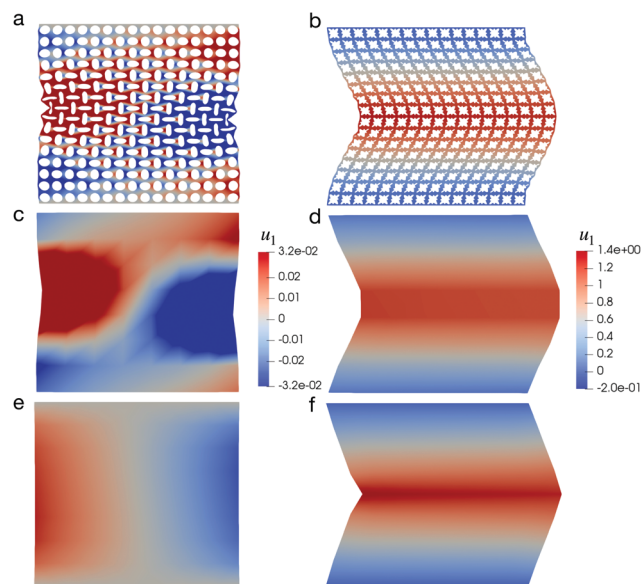**Fig. 9** Deformed configurations of CMMs with pore A (left column) and pore B (right column) under a 10% uniaxial compressive strain. Panels (a) and (b) are the results obtained from DNS, panels (c and d) are the RVE-averaged field of DNS, and panels (e and f) are obtained *via* the NN-based model. Color contours indicate the value of u_1 (displacement component along the $\mathbf{e}_1$ direction).

CMMs under an engineering strain of −10% are shown. Both DNS (Fig. 9a and b) and the NN-based model (Fig. 9e and f) have shown that even under the same compressive loads, the two CMMs develop very different shapes. We also computed the average displacement field over each RVE element of the CMMs using data from DNS. The results are shown in Fig. 9c and d.

Specifically for CMMs with pore A, as mentioned in Section 4.2, a negative Poisson's ratio is expected, *i.e.*, the compression in the e_2 direction will lead to a contraction also in the e_1 direction. This can be easily observed for the DNS results shown in Fig. 9a, where the CMM starts to contract in the middle region. The NN-based model also produces that result, as shown in Fig. 9e where displacement component u_1 is plotted. We can observe that it is positive on the left and negative on the right, which is a clear sign of contraction. As for CMMs with pore B, compression can lead to a bifurcation of the local microstructure, as mentioned in Section 4.2, which again can be observed from the DNS result in Fig. 9b. For the NN-based model, since the microstructural information has been averaged out, such bifurcation can only be inferred indirectly. Recall that in Fig. 5b, the two minima of $\overline{W}$ correspond to nonzero shear deformation with equal and opposite shear components. In Fig. 9f, we observe that under pure compression, the CMM develops a large local shear in the upper and lower part of the material, with opposite shear directions. The results in Fig. 9, whether obtained *via* DNS or the NN-based approach, are all in qualitative agreement with previous experimental work.[6]

Beyond visual qualitative comparisons, we obtained a stress–strain (σ–ε) curve for both CMMs to quantitatively assess the accuracy of our NN-based approach. The curves are obtained by varying the applied engineering strain ε from −10% to 10% and the results are shown in Fig. 10. The curves obtained from DNS and the NN-based model are almost identical for both pore A and pore B when under tension, even at large strain up to 10%. The NN-based model can reproduce the results of DNS for pore B for compression, but it starts to deviate from DNS results for pore A when the compression becomes large. This deviation is observed even with a much finer mesh for our NN-based approach.
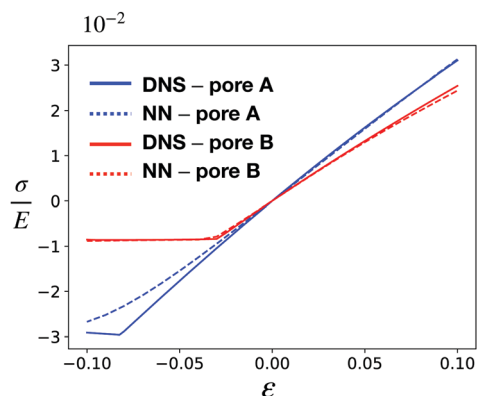

Fig. 10 Stress−strain curve for CMMs under uniaxial test with pore A (red) and pore B (blue) obtained *via* DNS (solid line) and the NN-based model (dashed line).

One possible reason for such behavior is the boundary effect. For CMMs with pore B we can observe some variation of microstructures near the boundary, but the variation is quite smooth and the main effect – the bifurcation into two shear states – is captured by the NN-based model. However for CMMs with pore A, on the left and right boundaries there are strong pore–boundary interactions, resulting in a drastic change in the pore shapes (see ESI†). This boundary effect persists even with the increasing number of composing unit cells. Another possible reason is that there is strong microstructure localization in the case of pore A. We can see that the rotation of the holes is drastic, and the distances between holes are small, thus leading to strong local interactions between the RVEs (Fig. 9a and ESI†). This is in contrast to the case of pore B, where pore rotations vary more smoothly yielding no strong localization (Fig. 9b and ESI†). Moreover, the strongly localized deformations in the case of pore A can lead to contacts between the interior boundaries of the pore, at which point our finite element model becomes invalid (without extension to handle contacts). In conclusion, the strong local variations in the microstructural features may impede the predictive power of our computational scheme. Possible ways of resolving this issue include using a separate model to account for the boundary effects,[81] or utilizing more advanced homogenization techniques to deal with the aforementioned localization effects.[32,33]

Aside from accuracy, we also compared the efficiency of the NN-based approach with DNS. Recall that one of our main motivations to construct such a surrogate-based approach is to reduce the computational complexity of DNS. This computational expense is mainly due to the fact that a small mesh size is needed to resolve the detailed cellular geometries, which results in a large number of degrees of freedom (DoF). Our NN-based model can use a much coarser mesh since the detailed microstructural features have already been averaged out and factored into the effective strain energy density. This significantly reduces the degrees of freedom when solving for the macroscopic behavior of the CMM – of course at the cost of losing the detailed local information of relevant fields. Table 1 summarizes the computational performance of DNS and the NN-based approach when they are used to generate the stress–strain curve in Fig. 10. The NN-based approach needs much fewer DoF to accurately capture the overall mechanics of the CMMs and hence can reduce the computational time by up to two orders of magnitude for both CMM with pore A and that with pore B. Note that for our problem, we used the same increment in ε to obtain the stress–strain curve. For a time-dependent problem, it is also important to examine the numerical stability of both approaches when different time steps are used.

6 Discussion

In the previous section, our NN-based approach is shown to efficiently predict the mechanical behavior of CMMs with homogeneous ξ but an inhomogeneous deformation field.

Table 1 Comparison of DoF (degrees of freedom) and computation time (in seconds) for DNS and NN with different pore shapes and loading conditions

	DoF	Computation time [s]
DNS – pore A – compression	158 310	5.15×10^2
DNS – pore A – tension		7.42×10^2
NN – pore A – compression	290	6.18
NN – pore A – tension		6.41
DNS – pore B – compression	139 520	5.33×10^2
DNS – pore B – tension		5.19×10^2
NN – pore B – compression	290	8.20
NN – pore B – tension		6.94

Here we further consider a CMM whose ξ is macroscopically inhomogeneous: $\xi(X) = \frac{X_2}{L}\xi_B + \left(1 - \frac{X_2}{L}\right)\xi_A$, a linearly varying ξ along the $\mathbf{e}_2$ direction. The shape of the CMM is still a square, with size $L = 16L_0$ and under the same uniaxial loading as described in Fig. 8. A maximum strain of 20% is applied to this CMM. Its deformed shape is shown in Fig. 11 when under a tensile strain of 20%. The macroscopic responses for both DNS and the NN-homogenized model agree with each other qualitatively by visual observation. When the applied $\varepsilon > 0$, i.e., tensile loading, we have found that the NN-based approach can reproduce the DNS results very well – as in the case of a CMM with homogeneous ξ. On the other hand, when under compression, the NN-based approach starts to diverge and fails to find a solution even at small compression.

We suggest two explanations for this phenomenon. First, since $\overline{W}$ is a strongly nonlinear function of ξ, especially when under compression, the ability of our neural network to capture that functional dependence remains uncertain, given that only two different ξ's (ξ_A and ξ_B) are included in the training data. Second, since the local mechanical properties of the CMM depend on ξ in a strongly nonlinear fashion, the ξ used in this study can still create a strong local variation. When the characteristic length of that variation is comparable to the RVE size, the assumption of separation of scales can break and in that case our multiscale framework will fail. Particularly in the above example, when the CMM is under uniaxial tension, as shown in Fig. 10, the mechanical properties of CMMs vary smoothly between different ξ's. Therefore, the NN-based

approach gives us good agreement with the DNS results in tension. However, when under compression, as the properties vary drastically between different ξ's, our NN-based approach starts to fail.

To enhance the fidelity of our NN-based approach for CMMs with complex pore shapes, it is useful to include a larger number of sampled ξ's in the database. This way, our neural networks can better capture the nonlinear dependence of $\overline{W}$ on the geometric parameters ξ. We can validate our results by conducting similar uniaxial tests on CMMs with a homogeneous ξ that are different from those in the training data and compare with DNS results. Once that dependence is established with good accuracy, we can use the NN-based approach to predict the mechanical behavior of CMMs with an arbitrary uniform ξ or those with a non-uniform ξ, which varies "smoothly enough".

However, for those ξ's that lead to large local variations and with characteristic lengths comparable to the size of RVE, our NN-based approach will fail since it breaks the basic assumption of our multiscale framework. For those CMMs, we have to rely on other approaches like DNS. We must be cautious about the spatial inhomogeneity of the problem that we are solving: be it either in the geometric features or in the deformation field. For the multiscale approach to work, we must ensure that those variations have a negligible influence on the macroscopic problems of interest. In principle, our NN-based multiscale approach only works when the size of the CMM is much larger than that of the RVE and when there is no strong localization effect.

In Section 5 we have demonstrated that our NN-based scheme can capture the mechanics of moderately sized CMMs with reasonable accuracy, but with significant computational savings over DNS. We anticipate further reduction for even larger CMM size. Nevertheless, it is worth noting that the most time-consuming step of our NN-based scheme is not solving the macroscopic problem using the NN-based model, but the generation of the training data. As reported in Section 4.1, it takes about 20 hours to construct the database, although it is trivially parallelizable. Even though it is time-consuming, this generation step is only required once, and the resulting NN-based model can be used to solve multiple problems. Therefore, significant time can still be saved compared to other multiscale methods like FE^2 where micro- and macroscopic problems have to be solved at the same time, as pointed out in ref. 53 and 54.

Owing to its great computational efficiency, the NN-based approach proposed in this work can be particularly useful for solving design problems – the reverse engineering of CMMs to achieve specific mechanical properties. Compared with typical multiscale approaches, our approach provides a straightforward way of evaluating the necessary derivatives needed for the sensitivity analysis,[82,83] once the functional dependence of $\overline{W}$ on ξ is well established. Therefore we envision that those powerful tools used for structural topological optimization of composite materials can now be used for the design of CMMs under the NN-based framework. However, since our NN-based multiscale approach only works for CMMs with smoothly
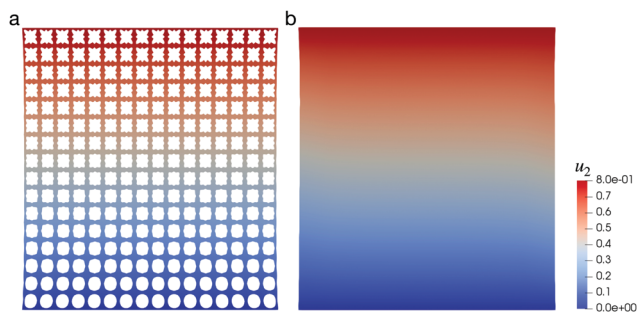
Fig. 11 Deformed configuration of a CMM with non-uniform pore shapes under a uniaxial tension of 20% obtained via (a) DNS and (b) the NN-based approach. Color contours indicate the value of u_2.

varying ξ, proper regularization has to be imposed to ensure that the optimal solution that we obtained does not violate that condition. Other structural parameters can also be included for the design of CMM, for example, the porosity of the CMM, the arrangement of the pores (other than the square arrays used in this work), *etc.*

Differentiability and fast deployment are two important motivators for choosing neural networks for this work. Other than neural networks and polynomial regression in Section 4.2, there are many machine learning techniques available, each suitable for different types of problems. For example, decision trees[84] are a popular machine learning technique which offers great interpretability; however they are not typically differentiable. Gaussian process regression can be an alternative to neural networks for small datasets, and can sometimes outperform neural networks in terms of accuracy. Yet, there can be great computational cost for deployment once the dataset becomes large.[85] The choice of machine learning techniques largely depends on the types of problems and applications considered. Sometimes multiple machine learning techniques can be combined together for optimal performance. In this work, our aim is to demonstrate that neural networks are a promising tool for the design of CMMs. There are limitations – the need to generate a large dataset, the need for smoothly varying ξ – but we expect that future work may be able to compose the model we present with other machine learning techniques to relax these restrictions.

7 Conclusion

In this work, we proposed a neural network based multiscale computational scheme which can be used to predict the overall mechanical behavior of cellular mechanical metamaterials under large deformation. Our scheme adopts a data-driven approach to estimate the functional dependence of the effective strain energy density on complex cellular geometries and finite overall deformation. We first identify a proper RVE of the cellular solid and build an offline training database by varying overall deformation as well as cellular geometries. The database is then used to train and validate a neural network model that can best represent the effective strain energy density as a function of cellular geometries and overall deformation. This neural network model is then treated as a coarse-grained constitutive model of the metamaterial and used to predict its overall mechanical behavior. Under certain conditions, our proposed scheme can significantly reduce the computational time compared with direct numerical simulation while achieving reasonable accuracy, especially when the metamaterial consists of a large number of unit cells. We discussed the limitations of the current scheme and emphasized the types of problems for which it is appropriate. Finally, we discussed the potential of using this to enable efficient rational design of metamaterials.

Conflicts of interest

There are no conflicts to declare.

Notes and references

1 L. J. Gibson and M. F. Ashby, *Cellular solids: structure and properties*, Cambridge University Press, 1999.
2 T. A. Schaedler and W. B. Carter, *Annu. Rev. Mater. Res.*, 2016, **46**, 187–210.
3 D. Chen and X. Zheng, *Sci. Rep.*, 2018, **8**, 9139.
4 S. Yuan, C. K. Chua and K. Zhou, *Adv. Mater. Technol.*, 2019, **4**, 1800419.
5 K. Bertoldi, P. M. Reis, S. Willshaw and T. Mullin, *Adv. Mater.*, 2010, **22**, 361–366.
6 J. T. Overvelde, S. Shan and K. Bertoldi, *Adv. Mater.*, 2012, **24**, 2337–2342.
7 J. T. Overvelde and K. Bertoldi, *J. Mech. Phys. Solids*, 2014, **64**, 351–366.
8 M. Mirzaali, S. Janbaz, M. Strano, L. Vergani and A. A. Zadpoor, *Sci. Rep.*, 2018, **8**, 965.
9 D. Krishnan and H. T. Johnson, *J. Mech. Phys. Solids*, 2009, **57**, 1500–1513.
10 L. R. Meza, S. Das and J. R. Greer, *Science*, 2014, **345**, 1322–1326.
11 X. Li and H. Gao, *Nat. Mater.*, 2016, **15**, 373.
12 B. Florijn, C. Coulais and M. van Hecke, *Soft Matter*, 2016, **12**, 8736–8743.
13 K. Bertoldi, V. Vitelli, J. Christensen and M. van Hecke, *Nat. Rev. Mater.*, 2017, **2**, 17066.
14 K. Bertoldi, *Annu. Rev. Mater. Res.*, 2017, **47**, 51–61.
15 E. Barchiesi, M. Spagnuolo and L. Placidi, *Math. Mech. Solids*, 2019, **24**, 212–234.
16 J. U. Surjadi, L. Gao, H. Du, X. Li, X. Xiong, N. X. Fang and Y. Lu, *Adv. Eng. Mater.*, 2019, **21**, 1800864.
17 M. M. Ameen, O. Rokoš, R. Peerlings and M. Geers, *Mech. Mater.*, 2018, **124**, 55–70.
18 E. Weinan, B. Engquist, X. Li, W. Ren and E. Vanden-Eijnden, *Commun. Comput. Phys.*, 2007, **2**, 367–450.
19 S. Ahuja, V. Yakhot and I. G. Kevrekidis, *Phys. Fluids*, 2008, **20**, 035111.
20 J. D. Eshelby, *Proc. R. Soc. A*, 1957, **241**, 376–396.
21 E. Kröner, *Z. Phys.*, 1958, **151**, 504–518.
22 Z. Hashin and S. Shtrikman, *J. Mech. Phys. Solids*, 1963, **11**, 127–140.
23 B. Budiansky, *J. Mech. Phys. Solids*, 1965, **13**, 223–227.
24 R. Hill, *J. Mech. Phys. Solids*, 1965, **13**, 213–222.
25 T. Mori and K. Tanaka, *Acta Metall.*, 1973, **21**, 571–574.
26 J. Willis, *J. Mech. Phys. Solids*, 1977, **25**, 185–202.
27 R. Hill, *J. Mech. Phys. Solids*, 1965, **13**, 89–101.
28 M. Berveiller and A. Zaoui, *J. Mech. Phys. Solids*, 1978, **26**, 325–344.
29 P. P. Castañeda, *J. Mech. Phys. Solids*, 1991, **39**, 45–71.
30 P. P. Castañeda, *J. Mech. Phys. Solids*, 1996, **44**, 827–862.

31 J. Segurado, R. A. Lebensohn and J. LLorca, *Advances in Applied Mechanics*, Elsevier, 2018, vol. 51, pp. 1–114.

32 M. G. Geers, V. G. Kouznetsova and W. Brekelmans, *J. Comput. Appl. Math.*, 2010, **234**, 2175–2182.

33 V. P. Nguyen, M. Stroeven and L. J. Sluys, *J. Multiscale Modell.*, 2011, **3**, 229–270.

34 S. Saeb, P. Steinmann and A. Javili, *Appl. Mech. Rev.*, 2016, **68**, 050801.

35 F. Feyel, *Comput. Mater. Sci.*, 1999, **16**, 344–354.

36 F. Feyel and J.-L. Chaboche, *Comput. Methods Appl. Mech. Eng.*, 2000, **183**, 309–330.

37 S. Ghosh, K. Lee and P. Raghavan, *Int. J. Solids Struct.*, 2001, **38**, 2335–2385.

38 K. Terada and N. Kikuchi, *Comput. Methods Appl. Mech. Eng.*, 2001, **190**, 5427–5464.

39 V. Kouznetsova, M. G. Geers and W. Brekelmans, *Comput. Methods Appl. Mech. Eng.*, 2004, **193**, 5525–5550.

40 J. Yvonnet and Q.-C. He, *J. Comput. Phys.*, 2007, **223**, 341–368.

41 H. Moulinec and P. Suquet, *C. R. Acad. Sci., Ser. IIb: Mec., Phys., Chim., Astron.*, 1994, **318**, 1417–1423.

42 H. Moulinec and P. Suquet, *Comput. Methods Appl. Mech. Eng.*, 1998, **157**, 69–94.

43 D. J. Eyre and G. W. Milton, *Eur. Phys. J.: Appl. Phys.*, 1999, **6**, 41–47.

44 J. Michel, H. Moulinec and P. Suquet, *CMES (Comput. Modell. Eng. Sci.)*, 2000, **1**, 79–88.

45 A. Gendy and A. Saleeb, *Comput. Mech.*, 2000, **25**, 66–77.

46 J. Yvonnet, E. Monteiro and Q.-C. He, *Int. J. Multiscale Comput. Eng.*, 2013, **11**, 201–225.

47 J. Yvonnet, D. Gonzalez and Q.-C. He, *Comput. Methods Appl. Mech. Eng.*, 2009, **198**, 2723–2737.

48 N. Takano, M. Zako and Y. Ohnishi, *J. Soc. Mater. Sci., Jpn.*, 1996, **45**, 81–86.

49 D. Ryckelynck, *J. Comput. Phys.*, 2005, **202**, 346–366.

50 I. Temizer and T. Zohdi, *Comput. Mech.*, 2007, **40**, 281–298.

51 R. Chowdhury, B. Rao and A. M. Prasad, *Commun. Numer. Methods Eng.*, 2009, **25**, 301–337.

52 F. Fritzen and O. Kunc, *Eur. J. Mech., A: Solids*, 2018, **69**, 201–220.

53 B. Le, J. Yvonnet and Q.-C. He, *Int. J. Numer. Meth. Eng.*, 2015, **104**, 1061–1084.

54 X. Lu, D. G. Giovanis, J. Yvonnet, V. Papadopoulos, F. Detrez and J. Bai, *Comput. Mech.*, 2019, **64**, 307–321.

55 S. Haykin, *Neural networks: a comprehensive foundation*, Prentice-Hall, Inc., 2007.

56 X. Glorot, A. Bordes and Y. Bengio, International Conference on Machine Learning, 2011, pp. 513–520.

57 A. Krizhevsky, I. Sutskever and G. E. Hinton, Neural Information Processing Systems, 2012, pp. 1097–1105.

58 D. Bahdanau, K. Cho and Y. Bengio, 2014, arXiv: 1409.0473.

59 J. Carrasquilla and R. G. Melko, *Nat. Phys.*, 2017, **13**, 431–434.

60 G. Carleo and M. Troyer, *Science*, 2017, **355**, 602–606.

61 D.-L. Deng, *Phys. Rev. Lett.*, 2018, **120**, 240402.

62 R. Gómez-Bombarelli, J. N. Wei, D. Duvenaud, J. M. Hernández-Lobato, B. Sánchez-Lengeling, D. Sheberla, J. Aguilera-Iparraguirre, T. D. Hirzel, R. P. Adams and A. Aspuru-Guzik, *ACS Cent. Sci.*, 2018, **4**, 268–276.

63 M. C. Chan and J. P. Stott, *Mon. Not. R. Astron. Soc.*, 2019, **490**, 5770–5787.

64 M. Wainberg, D. Merico, A. Delong and B. J. Frey, *Nat. Biotechnol.*, 2018, **36**, 829–838.

65 T. Xue, A. Beatson, S. Adriaenssens and R. P. Adams, *International Conference on Machine Learning*, 2020, pp. 8675–8684.

66 A. Beatson, J. T. Ash, G. Roeder, T. Xue and R. P. Adams, 2020, arXiv:2005.06549.

67 Z. Nie, H. Jiang and L. B. Kara, 2018, arxiv: 1808.08914.

68 K. Sagiyama and K. Garikipati, 2019, arxiv: 1901.00524.

69 H. Zhao, B. D. Storey, R. D. Braatz and M. Z. Bazant, *Phys. Rev. Lett.*, 2020, **124**, 060201.

70 R. Hill, *Proc. R. Soc. A*, 1972, **326**, 131–147.

71 T. Hastie, R. Tibshirani and J. Friedman, *The elements of statistical learning: data mining, inference, and prediction*, Springer Science & Business Media, 2009.

72 H. Robbins and S. Monro, *Ann. Math. Stat.*, 1951, 400–407.

73 D. E. Rumelhart, G. E. Hinton and R. J. Williams, *Learning internal representations by error propagation*, California univ san diego la jolla inst for cognitive science technical report, 1985.

74 F. Pedregosa, G. Varoquaux, A. Gramfort, V. Michel, B. Thirion, O. Grisel, M. Blondel, P. Prettenhofer, R. Weiss, V. Dubourg, J. Vanderplas, A. Passos, D. Cournapeau, M. Brucher, M. Perrot and E. Duchesnay, *J. Mach. Learn. Res.*, 2011, **12**, 2825–2830.

75 A. Logg, K.-A. Mardal and G. Wells, *Automated solution of differential equations by the finite element method: The FEniCS book*, Springer Science & Business Media, 2012, vol. 84.

76 I. M. Sobol', *Zh. Vychisl. Mat. Mat. Fiz.*, 1967, **7**, 784–802.

77 D. P. Kingma and J. Ba, 2014, arxiv: 1412.6980.

78 M. Stone, *J. R. Stat. Soc.: Ser. B (Methodological)*, 1974, **36**, 111–133.

79 C. M. Bishop, *Pattern recognition and machine learning*, Springer, 2006.

80 M. S. Alnæs, *Automated Solution of Differential Equations by the Finite Element Method*, Springer, 2012, pp. 303–338.

81 S. Sarkar, M. Cebron, M. Brojan and A. Kosmrlj, 2020, arXiv: 2004.01044.

82 G. Allaire, F. De Gournay, F. Jouve and A.-M. Toader, *Control Cybernetics*, 2005, **34**, 59.

83 H. A. Eschenauer and N. Olhoff, *Appl. Mech. Rev.*, 2001, **54**, 331–390.

84 L. Breiman, J. Friedman, C. J. Stone and R. A. Olshen, *Classification and regression trees*, CRC Press, 1984.

85 C. E. Rasmussen, *Summer School on Machine Learning*, 2003, pp. 63–71.